



Deposited via The University of Leeds.

White Rose Research Online URL for this paper:

<https://eprints.whiterose.ac.uk/id/eprint/228114/>

Version: Accepted Version

Article:

Cummins, D.P., Guemas, V., Blein, S. et al. (2024) Reducing Parametrization Errors for Polar Surface Turbulent Fluxes Using Machine Learning. *Boundary-Layer Meteorology*, 190. 13. ISSN: 0006-8314

<https://doi.org/10.1007/s10546-023-00852-8>

© The Author(s), under exclusive licence to Springer Nature B.V. 2024. This version of the article has been accepted for publication, after peer review (when applicable) and is subject to Springer Nature's AM terms of use (<https://www.springernature.com/gp/open-research/policies/accepted-manuscript-terms>), but is not the Version of Record and does not reflect post-acceptance improvements, or any corrections. The Version of Record is available online at: <https://doi.org/10.1007/s10546-023-00852-8>.

Reuse

Items deposited in White Rose Research Online are protected by copyright, with all rights reserved unless indicated otherwise. They may be downloaded and/or printed for private study, or other acts as permitted by national copyright laws. The publisher or other rights holders may allow further reproduction and re-use of the full text version. This is indicated by the licence information on the White Rose Research Online record for the item.

Takedown

If you consider content in White Rose Research Online to be in breach of UK law, please notify us by emailing eprints@whiterose.ac.uk including the URL of the record and the reason for the withdrawal request.

Reducing parametrization errors for polar surface turbulent fluxes using machine learning

Donald P. Cummins¹, Virginie Guemas¹, Sébastien Blein¹, Ian M.
Brooks², Ian A. Renfrew³, Andrew D. Elvidge³, and John Prytherch⁴

¹CNRM, Université de Toulouse, Météo-France, CNRS, Toulouse, France

²School of Earth & Environment, University of Leeds, Leeds, LS2 9JT,
UK

³School of Environmental Sciences, University of East Anglia, Norwich,
NR4 7TJ, UK

⁴Department of Meteorology, Stockholm University, Stockholm, Sweden

September 6, 2023

Abstract

Turbulent exchanges between sea ice and the atmosphere are known to influence the melting rate of sea ice, the development of atmospheric circulation anomalies and, potentially, teleconnections between polar and non-polar regions. Large model errors remain in the parametrization of turbulent heat fluxes over sea ice in climate models, resulting in significant uncertainties in projections of future climate. Fluxes are typically calculated using bulk formulae, based on Monin-Obukhov similarity theory, which have shown particular limitations in polar regions. Parametrizations developed specifically for polar conditions (e.g. representing form drag from ridges or melt ponds on sea ice) rely on sparse observations and thus may not be universally applicable.

23 In this study, new data-driven parametrizations have been developed for surface
24 turbulent fluxes of momentum, sensible heat and latent heat in the Arctic. Machine
25 learning has already been used outside the polar regions to provide accurate and
26 computationally inexpensive estimates of surface turbulent fluxes. To investigate
27 the feasibility of this approach in the Arctic, we have fitted neural-network mod-
28 els to a reference dataset (SHEBA). Predictive performance has been tested using
29 data from other observational campaigns. For momentum and sensible heat, per-
30 formance of the neural networks is found to be comparable to, and in some cases
31 substantially better than, that of a state-of-the-art bulk formulation.

32 These results offer an efficient alternative to the traditional bulk approach in
33 cases where the latter fails, and can serve to inform further physically based devel-
34 opments.

35 1 Introduction

36 Arctic sea ice has declined drastically over recent decades, drawing special attention and
37 instigating concern about potential repercussions on local ecosystems (Kovacs et al., 2011;
38 Post et al., 2013; Tynan, 2015), indigenous populations (Meier et al., 2014) and lower-
39 latitude climate (Cohen et al., 2014; Jung et al., 2015; Cohen et al., 2020; Liu et al., 2022).
40 Indeed, since the advent of satellite imagery, about three million km² of Arctic sea ice has
41 been lost; this represents a decrease by half of sea ice extent at the end of the summer
42 season and has coincided with a reduction in ice thickness also by about a half (Gascard
43 et al., 2019). Arctic sea ice loss is expected to continue in coming decades, although large
44 uncertainties still remain regarding the expected rate of disappearance (e.g. Bonan et al.,
45 2021a,b). Surface warming two to four times faster than the global mean has also been
46 observed in the Arctic over the last couple of decades (e.g. Cohen et al., 2014). This
47 phenomenon is commonly referred to as Arctic amplification (e.g. Serreze and Francis,
48 2006; Graversen et al., 2008; Serreze and Barry, 2011). Heat exchanges between the ice
49 and the atmosphere are a key determinant of both the rate of Arctic sea ice melting (e.g.
50 Rothrock et al., 1999; Screen and Simmonds, 2010) and the Arctic amplification (e.g.

51 Serreze et al., 2009; Lesins et al., 2012; Previdi et al., 2021).

52 Large uncertainties still remain in the estimation of surface turbulent fluxes under
53 polar-specific conditions (e.g. Vihma et al., 2014), where the atmospheric boundary layer
54 is frequently stable and turbulence can be intermittent (e.g. Andreas, 1998). Turbu-
55 lent fluxes are typically modelled through bulk formulae based on the Monin-Obukhov
56 similarity theory (Monin and Obukhov, 1954; Garratt, 1994; Andreas, 1998). Stability
57 corrections tailored to polar conditions have been proposed (Grachev et al., 2007) from
58 the year-long SHEBA (Surface Heat Budget of the Arctic Ocean, Uttal et al., 2002; Pers-
59 son et al., 2002) campaign, but the number of measurements used to produce them is
60 still limited compared to the volume of data available from tropical areas used to tailor
61 stability corrections for convective conditions. Polar-specific parametrizations have also
62 been proposed for surface roughness (e.g. Andreas, 1987; Andreas et al., 2010b; Andreas,
63 2011) and for the form drag arising from alternating floes and leads (e.g. Lüpkes et al.,
64 2012; Lüpkes and Gryanik, 2015; Elvidge et al., 2016). However, further calibration of
65 those parametrizations might still be necessary with upcoming campaigns (e.g. Elvidge
66 et al., 2021). Such parametrizations have been shown to reduce polar biases in atmo-
67 spheric models (Renfrew et al., 2019; Elvidge et al., 2023). Most climate models still use
68 a constant and fixed neutral transfer coefficient for all ice types and thicknesses (e.g. Notz
69 et al., 2013; Lüpkes et al., 2013). Reluctance to include the most up-to-date polar-specific
70 parametrizations in climate models has originated partly from the lack of observational
71 data available to validate and calibrate those parametrizations, and from inadequacies in
72 model formulation. This situation has improved with the recent Year of Polar Prediction
73 (Jung et al., 2016) and the MOSAiC campaign (Shupe et al., 2022), as well as other
74 studies using data gathered from recent intensive field campaigns in the Arctic (Elvidge
75 et al., 2016, 2021; Srivastava et al., 2022). Another obstacle to widespread adoption of
76 advanced schemes for specific situations (such as the presence of sea ice) may be the
77 fact that large-scale models have historically struggled to represent the stable boundary
78 layer, even in simple, homogeneous conditions (e.g. the GABLS experiments, Cuxart
79 et al., 2006; Svensson et al., 2011; Bosveld et al., 2014), although recent work suggests

80 that better parameter calibration is needed (Audouin et al., 2021). Finally, both the
81 stability correction and the surface roughness parametrizations, which are essential com-
82 ponents of the Monin-Obukhov similarity theory leading to estimates of surface turbulent
83 fluxes, depend on the surface turbulent fluxes themselves. Hence, iterative algorithms are
84 often used (Fairall et al., 2003; Edson et al., 2004). Calibration of such algorithms on
85 noisy data is complicated by the “self-correlation” phenomenon (e.g. Baas et al., 2006).

86 Some of those challenges could be bypassed through the use of machine-learning al-
87 gorithms, a type of empirical “black box” relating the turbulent fluxes directly to the
88 observable meteorological quantities on which they depend. Although somewhat lacking
89 in physical interpretability, the data-driven approach avoids the many sequential steps
90 involved in developing bulk schemes, which are likely to result in compounding errors.
91 There is also the possibility of assessing the effect of input variables not directly included
92 in the physical relationships of the bulk method. Most importantly, machine-learning
93 models have the potential to deliver more accurate flux estimates. The observational
94 data collected thus far offer the opportunity to assess the relevance of such an approach.
95 Machine learning has already been tested for the estimation of surface turbulent fluxes
96 outside the polar regions with a successful outcome (e.g. Pelliccioni et al., 1999; Qin et al.,
97 2005a,b; Wang et al., 2017; Safa et al., 2018; Xu et al., 2018; Leufen and Schädler, 2019;
98 Wang et al., 2021). In recent studies, machine-learning parametrizations have been de-
99 veloped which can accurately estimate turbulent fluxes observed at measurement towers
100 (McCandless et al., 2022; Wulfmeyer et al., 2022), and the properties of such parametriza-
101 tions investigated in large-eddy simulations (Muñoz-Esparza et al., 2022). In this study,
102 we apply data-driven methods to the SHEBA campaign to investigate the viability of this
103 approach in polar conditions, and we assess its performance compared to a state-of-the-
104 art bulk formulation over a few other recent Arctic campaigns. This article is structured
105 as follows. Section 2 describes the available field data used to carry out our analysis.
106 Section 3 presents the bulk- and the data-driven approaches to estimate surface turbu-
107 lent fluxes as well as the statistical methodology to assess their performance. Section 4
108 describes the results. Conclusions and perspectives are provided in Section 5.

2 Data

Our analyses make use of data from the following observational campaigns.

- SHEBA (Surface Heat Budget of the Arctic Ocean): the SHEBA ice camp was set up around the icebreaker *Des Groseilliers*, which was frozen into the Arctic ice pack and drifted approximately 2700 km in the Beaufort Gyre between 2 October 1997 and 11 October 1998. It started in the Beaufort Sea, drifted westward into the Chukchi Sea, then turned north into the Arctic Ocean near the date line. Turbulent fluxes and mean meteorological data were measured continuously at five levels: 2.2, 3.2, 5.1, 8.9, and 18.2 m (or 14 m during most of the winter), on the 20-metre main SHEBA tower. Turbulent covariances and variances were estimated at each level based on one-hour averaging and derived through the frequency integration of the cospectra and spectra (Persson et al., 2002). From the more than 8000 h for which the main SHEBA tower was instrumented, over 6000 h passed quality control. Four remote sites, ranging in distance from 0.25 to 30 km from the main camp and known as Portable Automated Mesonet (PAM) stations, were also instrumented. The PAM stations provided measures of wind, temperature and humidity together with estimates of surface heat fluxes through eddy covariances. The sea ice characteristics changed radically during the year-long deployment, from compact and snow-covered in winter (Andreas et al., 2010b), through to a covering littered with deep melt ponds and leads in summer (Andreas et al., 2010a). Other details of the SHEBA programme, the ice camp, deployed instruments, data processing, accuracy, calibration, and archived data files may be found in Andreas et al. (1999, 2002, 2003, 2006); Persson et al. (2002); Uttal et al. (2002); Grachev et al. (2002, 2005).
- ACCACIA (Aerosol-Cloud Coupling and Climate Interactions in the Arctic): eight flights, from 21 to 31 March 2013, to the northwest of Svalbard over the Fram Strait and to the southeast of Svalbard in the Barents Sea, were conducted with two aircraft: a DHC6 Twin Otter operated by the British Antarctic Survey and equipped

137 with the Meteorological Airborne Science Instrumentation (MASIN) (King et al.,
138 2008; Fiedler et al., 2010); and the UK Facility for Airborne Atmospheric Mea-
139 surement (FAAM) BAe-146 (Renfrew et al., 2008; Petersen and Renfrew, 2009).
140 Both aircraft measured turbulent fluxes and meteorological parameters in the at-
141 mospheric boundary layer, as well as surface meteorological parameters through
142 radar, leading to more than 200 new estimates of surface drag in the Marginal Ice
143 Zone (Elvidge et al., 2016). In the Barents Sea, sea ice was characterized by small,
144 unconsolidated ice floes (generally associated with a higher neutral drag coefficient),
145 while over the Fram Strait there were typically larger, smoother floes (Elvidge et al.,
146 2016).

- 147 • ACSE (Arctic Cloud in Summer Experiment): the icebreaker *Oden* left Tromsø,
148 Norway, on 5 July 2014, crossing the Kara, Laptev, East Siberian, and Chukchi
149 Seas, following the Siberian Shelf, and arriving in Barrow, Alaska, on 18 August.
150 A second leg left Barrow on 21 August following a similar route back, albeit farther
151 north. The expedition ended on 5 October in Tromsø. An instrumented mast
152 at the bow of the ship was used to obtain surface turbulent fluxes through the
153 eddy covariance technique (Prytherch et al., 2017; Thornton et al., 2020; Srivastava
154 et al., 2022), while a weather station on the seventh deck at about 25 m measured
155 temperature, humidity and wind (Sotiropoulou et al., 2016). The 12-week ACSE
156 cruise took place within the Arctic pack ice, working over, and just off the Siberian
157 Shelf, during summer melt and early autumn freeze-up conditions. It sampled a
158 wide range of sea ice morphologies (Persson et al., 2015; Srivastava et al., 2022).
- 159 • AO16 (Arctic Ocean 2016): the icebreaker *Oden* departed from Longyearbyen,
160 Svalbard, on 8 August and operated in the Arctic Ocean, mainly in the Amundsen
161 Basin and in areas around the underwater mountain ranges, Lomonosov Ridge and
162 Alpha Ridge, until 19 September 2016. Similar instrumentation as in the ACSE
163 expedition was employed (Tjernström and Jakobsson, 2021; Srivastava et al., 2022).
164 The six-week AO16 cruise followed a more northerly route than ACSE (mostly
165 north of 85°N) and the surface was mostly characterized by old and thick ice, with

166 intermittent patches of thin ice and melt ponds (Srivastava et al., 2022).

167 Corresponding estimates of sea ice concentration from satellite imagery were obtained
168 from the National Snow and Ice Data Center (NSIDC, Meier et al., 2021). For the
169 AO16 dataset, the included satellite-based estimates were used. See the data availability
170 statement for details of where to obtain the datasets used in this study.

171 **3 Methods**

172 **3.1 Bulk flux parametrizations**

Sea ice, atmosphere and coupled climate models rely on Monin-Obukhov Similarity Theory (MOST, Monin and Obukhov, 1954) to represent turbulent fluxes at the surface-atmosphere interface through bulk flux parametrizations. The bulk approach consists in estimating surface turbulent fluxes of momentum τ , sensible heat H_S and latent heat H_L from the near-surface gradient of model-resolved (or averaged) variables (wind speed, temperature and humidity), weighting each gradient by the corresponding transfer coefficient for momentum (C_D , the drag coefficient), sensible heat (C_H) and latent heat (C_q):

$$|\tau| = \rho C_D(z) u(z)^2, \quad (1)$$

$$H_S = \rho c_p C_H(z) u(z) (\theta_s - \theta(z)), \quad (2)$$

$$H_L = \rho L_v C_q(z) u(z) (q_s - q(z)), \quad (3)$$

173 where ρ is the air density, u is the horizontal component of wind, θ is the potential
174 temperature, q is the specific humidity, c_p is the specific heat of air at constant pressure,
175 L_v is the latent heat of vaporization or sublimation, C_D , C_H and C_q are the transfer
176 coefficients which all depend on the height z at which the wind speed u , the temperature
177 θ and the humidity q are taken, θ_s is the surface potential temperature and q_s is the
178 surface humidity.

179 A bulk parametrization essentially consists of an algorithm estimating the transfer

180 coefficients C_D , C_H and C_q . In this study, we use a composite bulk algorithm comprising
181 recent components developed for use in polar conditions. Over the ocean, we use the
182 COARE 3.0 algorithm (Fairall et al., 2003; Edson et al., 2013), with a first guess of
183 transfer coefficients deduced from the stability according to Grachev and Fairall (1997)
184 to speed up the convergence, stability correction for unstable conditions from Grachev
185 et al. (2000), and for stable conditions from Beljaars and Holtslag (1991), the aerodynamic
186 roughness model from Edson et al. (2013) and the scalar roughness model from Fairall
187 et al. (2003). The COARE 3.0 algorithm has been extensively tested and is currently
188 used in large-scale climate models (e.g. CNRM-CM6, Voltaire et al., 2019).

189 Over sea ice, the stability correction under stable conditions relies on Grachev et al.
190 (2007), the scalar roughness model on Andreas (1987) and the aerodynamic roughness
191 model on Andreas et al. (2010b), the rest of the algorithm being the same as over the
192 ocean (i.e. COARE 3.0). Sea ice concentrations between zero and unity are handled by
193 taking a weighted average of the estimated fluxes over ocean and sea ice, weighting by sea
194 ice concentration. This averaging approach, known as the *mosaic* method (e.g. Vihma,
195 1995), is already used in general circulation models (GCMs), such as CNRM-CM6. For
196 the momentum flux, we also include a form drag contribution, which accounts for the
197 increased turbulence observed where floes and leads are alternating (Lüpkes and Gryanik,
198 2015). This combination leads to the best estimates of surface turbulent fluxes that we
199 can obtain in light of the most recent studies focusing on polar regions (Andreas et al.,
200 2010a,b; Lüpkes and Gryanik, 2015; Elvidge et al., 2016; Srivastava et al., 2022). On the
201 datasets used in this study, momentum flux estimates from our polar-specific algorithm
202 have up to 23 % lower root-mean-square error (RMSE) than those from the unmodified
203 COARE 3.0. Estimated heat fluxes are very similar with or without the polar-specific
204 modifications (corr. > 0.99). The bulk algorithm described here is publicly available
205 for download as a Python library (see the code availability statement for a link to the
206 repository) and the equations of the polar-specific components are given in the appendix.

Following the MOST, surface turbulent fluxes are commonly expressed as functions
of the scaling parameters u_* , θ_* and q_* for wind, potential temperature and humidity

respectively:

$$|\tau| = \rho u_{\star}^2, \tag{4}$$

$$H_S = -\rho c_p u_{\star} \theta_{\star}, \tag{5}$$

$$H_L = -\rho L_v u_{\star} q_{\star}. \tag{6}$$

207 So-called kinematic fluxes u_{\star}^2 , $u_{\star} \theta_{\star}$ and $u_{\star} q_{\star}$ will be used in the remainder of this study
 208 because they correspond directly to the eddy covariances which are measured in the field.

209 3.2 Neural networks

210 Multiple machine-learning algorithms were tested for this study including random forests
 211 (Breiman, 2001), gradient boosting machines (Friedman, 2001; Chen and Guestrin, 2016),
 212 generalized additive models (Hastie and Tibshirani, 1986) and multivariate adaptive re-
 213 gression splines (Friedman, 1991). In general, it was found that algorithms permitting
 214 high-degree interactions between input variables performed better, but often at the cost
 215 of many free parameters. The algorithm chosen for the final analysis was the artificial
 216 neural network, which we found to offer the best predictive performance and with a
 217 relatively parsimonious model.

218 Neural networks can approximate continuous functions of multiple variables (Hornik
 219 et al., 1989) and have performed well in previous studies as estimators of surface tur-
 220 bulent fluxes (Pelliccioni et al., 1999; Qin et al., 2005a; Wang et al., 2017; Safa et al.,
 221 2018; Xu et al., 2018; Leufen and Schädler, 2019; McCandless et al., 2022; Muñoz-Esparza
 222 et al., 2022; Wulfmeyer et al., 2022). Many specialized configurations of network nodes
 223 or *architectures* have been developed for specific applications, for example the convolu-
 224 tional networks used for image recognition (e.g. Krizhevsky et al., 2017), however in this
 225 study attention is restricted to the simplest architecture: the single-layer feed-forward
 226 network. At its most basic, a neural network is a non-linear generalization of linear re-
 227 gression, in which the independent and dependent variables are represented as input and
 228 output nodes. A feed-forward network passes information from a layer of input nodes, by

229 way of linear combination, to a so-called hidden layer, containing nodes with non-linear
 230 activation functions (see Figure 1). An activation function is simply a non-linear trans-
 231 formation. Finally, the output of the hidden layer is combined in the output layer, which
 232 in our case consists of a single node representing the estimated flux. For an introduction
 233 to feed-forward neural networks see Ripley (1996).

234 Let x_i denote a seven-element input vector containing measurement height z , wind
 235 speed $u(z)$, potential temperature $\theta(z)$, surface temperature θ_s , specific humidity $q(z)$,
 236 surface humidity q_s and sea ice concentration C_i . These are the predictor variables used
 237 as inputs to the bulk algorithm described above. Letting $y \in \{u_\star^2, u_\star\theta_\star, u_\star q_\star\}$ denote the
 238 flux of interest in kinematic units, we can write a network-predicted flux \hat{y} as

$$\hat{y} = \alpha_0 + \sum_{j=1}^{N_j} w_j f \left(\alpha_j + \sum_{i=1}^7 w_{ji} x_i \right), \quad (7)$$

239 where, in neural-network parlance, constants α_j are known as biases, coefficients w_{ji} are
 240 weights, and f is a non-linear activation function. Here we use the sigmoid activation
 241 $f(x) = e^x / (1 + e^x)$. The number of hidden nodes N_j controls the total number of
 242 parameters and hence the complexity of the network. In practice, it is necessary to rescale
 243 the inputs and outputs, to avoid excessive saturation of each hidden node's activation
 244 function (Ripley, 1996). Saturation refers here to the disappearing gradient of the sigmoid
 245 function for inputs with large magnitude. We rescale all variables for model training via
 246 z-score normalization.

247 Training of the neural networks was performed by minimizing the sum of squared
 248 prediction errors on a designated training set. The sum of squared errors was minimized
 249 using the implementation of the Broyden-Fletcher-Goldfarb-Shanno (BFGS, Broyden,
 250 1970; Fletcher, 1970; Goldfarb, 1970; Shanno, 1970) quasi-Newton method in the *nnet*
 251 package for R (Venables and Ripley, 2002; R Core Team, 2021). Numerical optimization of
 252 the network parameters requires a non-zero initialization of the weights and biases, which
 253 is obtained by random number generation. Due to the presence of local minima in the
 254 least-squares objective function to be minimized, such random initialization introduces
 255 randomness in the fitted networks, making it difficult to measure predictive performance.

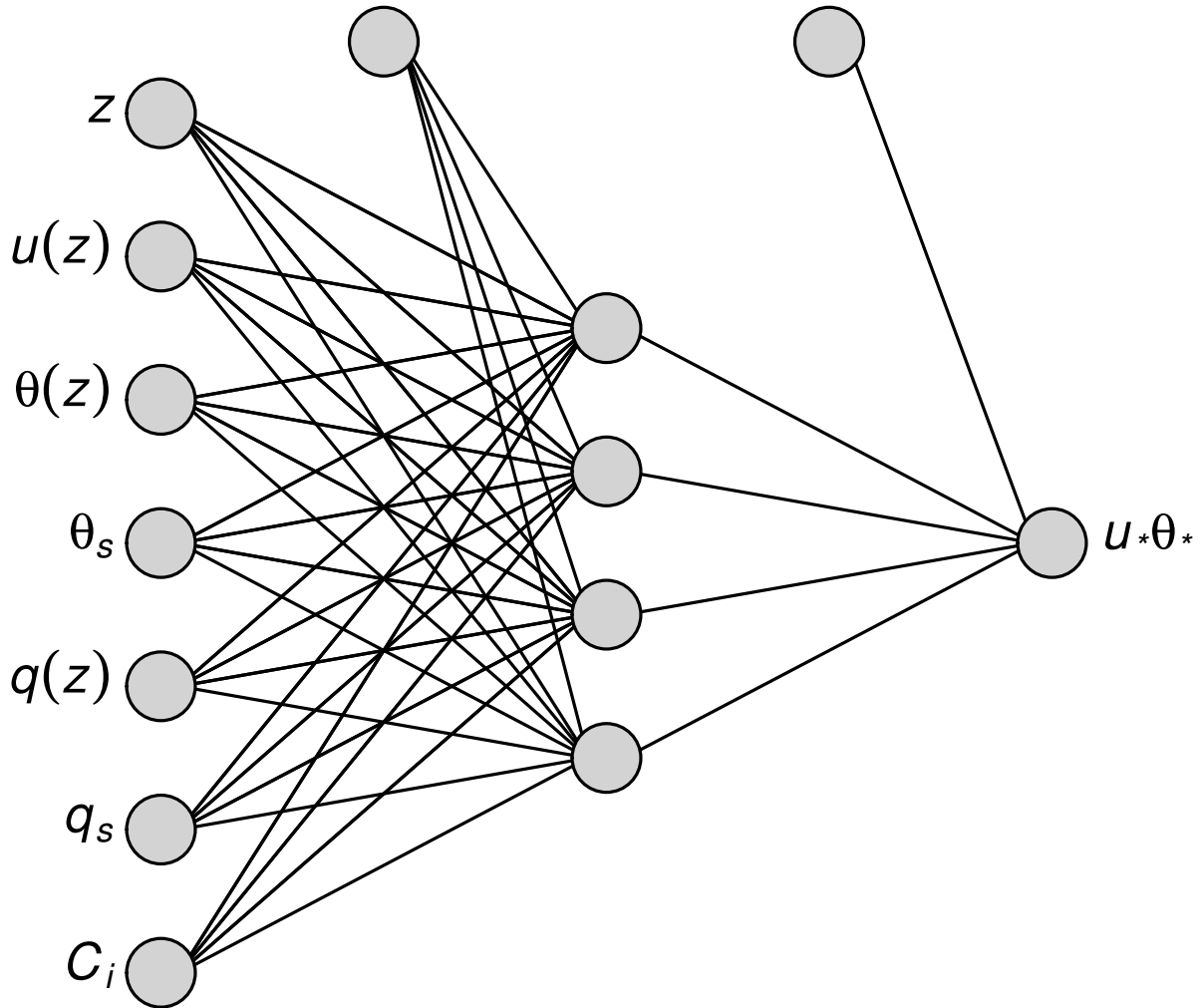


Figure 1: Neural-network architecture schematic. Information is passed from the seven inputs nodes on the left, through the four hidden nodes with non-linear activation functions, to the output node - in this case kinematic sensible heat flux $u_*\theta_*$. Separate networks with the same architecture were estimated for fluxes of momentum u_*^2 and latent heat u_*q_* . The two unlabelled nodes at the top correspond to node biases (analogous to the intercept term in a linear regression) and represent constant inputs of value unity.

256 Following Ripley (1996) we take two steps to address this problem. Firstly, applying a
257 quadratic penalty to the network weights (a technique known as weight decay, L2 regular-
258 ization or Tikhonov regularization) constrains the weights to be small in magnitude and
259 increases the convexity of the objective, thus improving the numerical conditioning of the
260 minimization problem. Secondly, we fit each neural network 100 times, each time using
261 an independent random parameter initialization. The set of 100 fitted networks is used
262 as a model ensemble, with an overall prediction obtained by averaging predictions from
263 all the members. Thus we largely eliminate randomness in our results due to parameter
264 initialization, and at the same time we gain a small boost in mean predictive performance
265 compared with using single networks. The performance gain from ensemble averaging is
266 sufficiently small ($< 5\%$ reduction in RMSE) that, for implementation in a GCM, the
267 improvement over single networks may not be worth the computational cost.

268 The neural networks in this study have two tunable hyperparameters: N_j , the number
269 of nodes in the hidden layer; and λ , the L2 regularization penalty. Setting $\lambda = 0.01$, at the
270 upper bound of the range recommended by Ripley (1996), and $N_j = 4$ gives the networks
271 more than enough flexibility to emulate their respective bulk-algorithm counterparts over
272 the range of meteorological conditions observed. Since the bulk algorithm represents an
273 *a priori* estimate of the functions to be approximated by the network, it makes sense
274 to use the bulk in this way when choosing the model complexity. Aggressive tuning
275 of hyperparameters using observational data has been avoided, so as not to excessively
276 bias the cross-validation results (see Section 3.3), although it should be noted that these
277 settings are roughly optimal. Increasing N_j beyond four does not substantially improve
278 performance for any of the fluxes considered, while the chosen value of λ is sufficient
279 to keep network weights within a suitable range for the sigmoid activation (standard
280 deviation of order unity).

281 Our approach to neural-network modelling of surface turbulent fluxes differs in some
282 ways from recent studies by other authors. For example, McCandless et al. (2022),
283 Muñoz-Esparza et al. (2022) and Wulfmeyer et al. (2022) employ deep networks, i.e.
284 networks containing multiple hidden layers, as well as more nodes per layer, resulting in

285 models with orders of magnitude more parameters. The rationale behind that approach is
286 to equip the network with a huge learning capacity (flexibility to approximate functions),
287 thus ruling out any possibility of underfitting. To mitigate the corresponding tendency of
288 larger models to overfit, those studies used a reduced number of training iterations. The
289 network architecture used in this study is more similar to that of Leufen and Schädler
290 (2019), who found that single-layer networks with just a handful of nodes provide a good
291 balance of parsimony and flexibility for modelling turbulent fluxes. Indeed, the purpose of
292 regularization techniques, such as early stopping during training, is to reduce the effective
293 degrees of freedom of the model (Hastie et al., 2009). Since the ultimate goal is to obtain
294 parametrizations suitable for use in a GCM, where redundant computation should be
295 avoided wherever possible, we therefore favour smaller, more highly optimized networks.
296 The neural-network parametrization of Leufen and Schädler (2019) had roughly the same
297 computational cost as a bulk algorithm based on the MOST, when implemented in a
298 one-dimensional land surface model.

299 Our model also differs from those in the above studies in our choice of input variables
300 to the network. Specifically, network inputs in the present study were constrained to
301 be the same variables used as inputs to the bulk algorithm. This restriction allows
302 a fair apples-to-apples comparison of the performance of the different parametrizations.
303 Wulfmeyer et al. (2022) use incoming and outgoing radiation as predictor variables. While
304 we second their finding that the radiation terms contribute explanatory power to predict
305 fluxes, we have refrained from including them in our parametrizations. This is because the
306 surface radiation balance in a GCM is itself dependent on complicated radiative transfer
307 parametrizations, which means that including radiation terms in a turbulent flux model
308 risks introducing another layer of compounding errors. We have also refrained from pre-
309 computing gradients of temperature and humidity, or other derived quantities such as
310 the bulk Richardson number. Instead, by including measurement height z as a model
311 input, we allow any explicit height dependence of the fluxes to be modelled empirically.
312 Thus we avoid interpolating observations to reference heights, which would anyhow be
313 impossible (given that, except at the SHEBA tower, most of the variables were measured

314 at only one height above ground level) without making parametric assumptions on the
315 vertical profiles (e.g. the MOST). From the ACCACIA flight data, only those fluxes
316 observed at altitudes below 30 m have been used in model training and validation, due
317 to concern about how representative the higher-altitude observations (up to 90 m) are of
318 surface-layer conditions. The first model level in GCMs, e.g. CNRM-CM6, is typically
319 well below 30 m over ocean.

320 **3.3 Cross validation**

321 The purpose of the present study is to determine whether a machine-learning algorithm,
322 trained on observational data collected in the Arctic, can offer improved performance over
323 advanced bulk formula parametrizations developed for use in polar regions. An important
324 property of neural-network models is that they can often achieve an arbitrarily high
325 goodness-of-fit on the training data, simply by increasing the number of free parameters
326 in the model (Hastie et al., 2009). Therefore, when observations contain measurement
327 errors, as is usually the case, one must be careful not to overfit the data (extract not only
328 signal but also noise). To mitigate the risk of overfitting, the performance of a machine-
329 learning model should be assessed based on its ability to predict *unseen* data (data not
330 used to train the model), hereafter the “out-of-sample” performance. A popular approach
331 to measuring out-of-sample performance is K -fold cross validation, which entails splitting
332 the data into K independent subsets. For each $k \in \{1, \dots, K\}$, the model is fitted to
333 those data *not* contained in subset k . The fitted model is then used to predict the
334 response variable in subset k . Iterating over the K subsets, one thus obtains a complete
335 dataset of out-of-sample predictions from which to compute performance metrics such as
336 root-mean-square error (RMSE) or mean absolute error (MAE).

337 Statistical independence of the K subsets is a necessary condition for cross-validated
338 performance metrics to be meaningful. In a typical machine-learning problem, genuinely
339 independent subsets are not available and are instead manufactured by randomly parti-
340 tioning a single dataset into K folds. Datasets of surface turbulent fluxes are typically
341 measured as time series, in our case none longer than a year, which invalidates the inde-

pendence assumption of the random subsetting approach. While one alternative would be to construct an elaborate stratified cross-validation scheme, intended to account for temporal (and other sources of) autocorrelation, we instead opt to make use of the fact that in this study we have a database of observations from multiple field campaigns. The observations were collected at a range of locations, at different times, using different measurement instruments, by different teams of researchers and under different meteorological conditions. For example, data were collected at towers, from ship masts and from low-flying aircraft. In theory, cross validation of a flux parametrization across observational campaigns estimates how well we would expect it to perform at predicting data collected in a future campaign, which would seem an appealingly objective metric for comparison. In practice, however, there are some limitations on the independence of the available datasets. For example, overlap in the large-scale meteorological conditions at the SHEBA tower and SHEBA PAM stations cannot be ruled out as a potential source of statistical dependence. Nevertheless, the degree of heterogeneity in the present ensemble of datasets is such that achieving a generalizable parametrization may be regarded as a real benchmark of success.

3.4 Variable importance

One advantage of supplying the same input variables to the neural networks as to the bulk algorithm is that the two methods can be diagnosed and compared using *variable importance* techniques. Wulfmeyer et al. (2022) used the so-called “feature importance” methodology proposed in Breiman (2001) to compare two machine-learning algorithms for computing surface turbulent fluxes. The feature importance algorithm is as follows. Firstly, a model is used to make predictions on a dataset and the quality of those predictions is assessed using some error metric (e.g. MSE). Then, for each input variable to the model x_i , the values of that variable are randomly shuffled in the dataset and the model predictions (and corresponding error metrics) recomputed. The importance of each input variable is estimated as the respective amount by which the performance metric increases when that variable is shuffled. This procedure has been applied to the

Table 1: Cross-validated performance metrics of neural-network (nnet) and bulk-algorithm flux parametrizations in kinematic units. The cross validation was over observational campaigns. Boldface indicates a significantly better score at the five-percent level in one of root-mean-square error (RMSE), mean absolute error (MAE) or Pearson correlation.

	campaign	n	RMSE		MAE		corr.	
			bulk	nnet	bulk	nnet	bulk	nnet
u_*^2	accacia	65	0.085	0.247	0.047	0.234	0.57	0.49
	acse	2324	0.053	0.051	0.036	0.035	0.83	0.80
	ao16	250	0.090	0.072	0.063	0.044	0.82	0.90
	sheba_atlanta	3203	0.019	0.019	0.012	0.011	0.91	0.91
	sheba_baltimore	279	0.036	0.038	0.021	0.022	0.64	0.65
	sheba_csm	225	0.029	0.029	0.019	0.019	0.89	0.88
	sheba_florida	427	0.048	0.047	0.031	0.031	0.82	0.82
	sheba_tower	23028	0.018	0.021	0.011	0.014	0.95	0.93
$u_*\theta_*$	accacia	50	0.0214	0.0476	0.0163	0.0273	0.95	0.61
	acse	796	0.0095	0.0115	0.0064	0.0083	0.85	0.81
	ao16	95	0.0154	0.0135	0.0102	0.0093	0.58	0.73
	sheba_atlanta	3203	0.0063	0.0055	0.0040	0.0035	0.65	0.64
	sheba_baltimore	279	0.0061	0.0062	0.0043	0.0050	0.48	0.45
	sheba_csm	225	0.0202	0.0177	0.0093	0.0085	0.00	0.01
	sheba_florida	427	0.0141	0.0132	0.0102	0.0093	0.29	0.32
	sheba_tower	23633	0.0037	0.0061	0.0025	0.0046	0.82	0.47
u_*q_*	accacia	34	2.85E-06	7.96E-06	1.76E-06	6.24E-06	0.97	0.72
	acse	673	1.03E-05	1.05E-05	5.93E-06	6.24E-06	0.35	0.17
	ao16	81	1.44E-05	1.46E-05	6.27E-06	5.58E-06	0.24	0.10
	sheba_tower	13511	1.06E-06	5.72E-06	5.51E-07	4.03E-06	0.69	-0.23

370 bulk algorithm and neural-network models used in this study, and the resulting variable
371 importances scaled to lie between zero and unity.

372 4 Results

373 Performance metrics computed from the cross-validation experiments are given in Table
374 1. Measured differences in performance between the bulk and neural-network methods
375 were tested for statistical significance on a per-dataset basis using a bootstrapping ap-
376 proach (Davison and Hinkley, 1997). Model-predicted turbulent fluxes in kinematic units
377 are plotted against field observations from the ACSE dataset in Figure 2. Results for

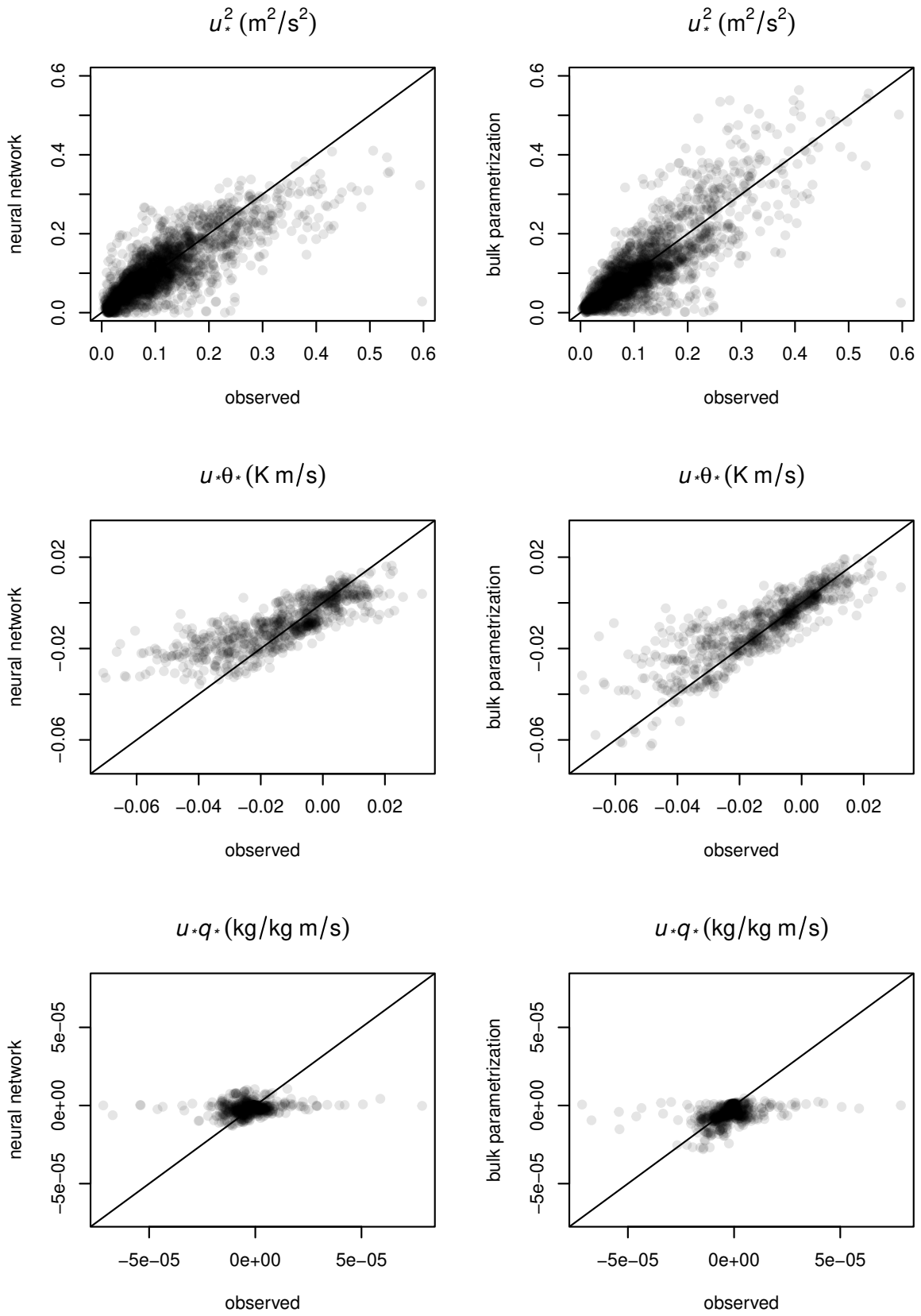


Figure 2: Scatter plots of predicted vs observed fluxes in kinematic units for the ACSE campaign. The diagonal line has equation $y = x$ and represents 100 % predictive accuracy.

378 ACSE are fairly representative of the results across the other datasets, with the notable
379 exception of the ACCACIA flight data. Equivalent figures for the other datasets, in-
380 cluding ACCACIA, are provided in the supplementary information. Computed variable
381 importance metrics for the bulk algorithm and neural-network models are shown in Figure
382 3.

383 It can be seen from these results that, of the three turbulent fluxes $\{u_*^2, u_*\theta_*, u_*q_*\}$,
384 the momentum flux u_*^2 is by far the easiest to predict, due to its strong linear correlation
385 with squared wind speed u^2 . Compared with the bulk algorithm, the neural-network
386 model performs similarly well or better on most datasets, except for ACCACIA and
387 the SHEBA tower. Performance at the SHEBA tower is expected to be worse because
388 that dataset accounts for most of the available observations and removing it reduces the
389 training set to a small fraction of its former size. In ACCACIA, the neural-network
390 model systematically overpredicts u_*^2 , in an unsuccessful attempt to extrapolate beyond
391 the range of measurement heights z seen in the training set. Note that z in ACCACIA
392 ranges from 20 to 30 m, while the highest z in the other datasets is $z = 20.3$ m in ACSE
393 and AO16. The greatest proportional error reduction was seen in the AO16 dataset where
394 the neural-network model gave a 21 % reduction in RMSE. In general, bulk estimates of
395 u_*^2 are very good, so there is little room for large performance improvements, especially
396 considering the fact that we are dealing with noisy real-world observations. There is a
397 notable negative bias in the neural-network estimates for large values of u_*^2 in the ACSE
398 dataset (see Figure 2), which is an artifact of the conservative extrapolatory properties
399 of neural networks (see next paragraph). It should be noted that the bulk algorithm
400 exhibits a similar negative bias in other datasets, e.g. AO16. Due to the lack of boundary
401 constraints on its output, the neural-network model occasionally produces very small
402 negative estimates of u_*^2 . In this study, such estimates have been rounded up to zero
403 before computing performance metrics, as this step can easily be included when the
404 parametrization is implemented in a GCM. Estimation of u_*^2 in a log-transformed space,
405 a common method for enforcing strict positivity, is inappropriate here, since in a GCM it
406 is the magnitude of the flux in an absolute rather than relative sense which is important.

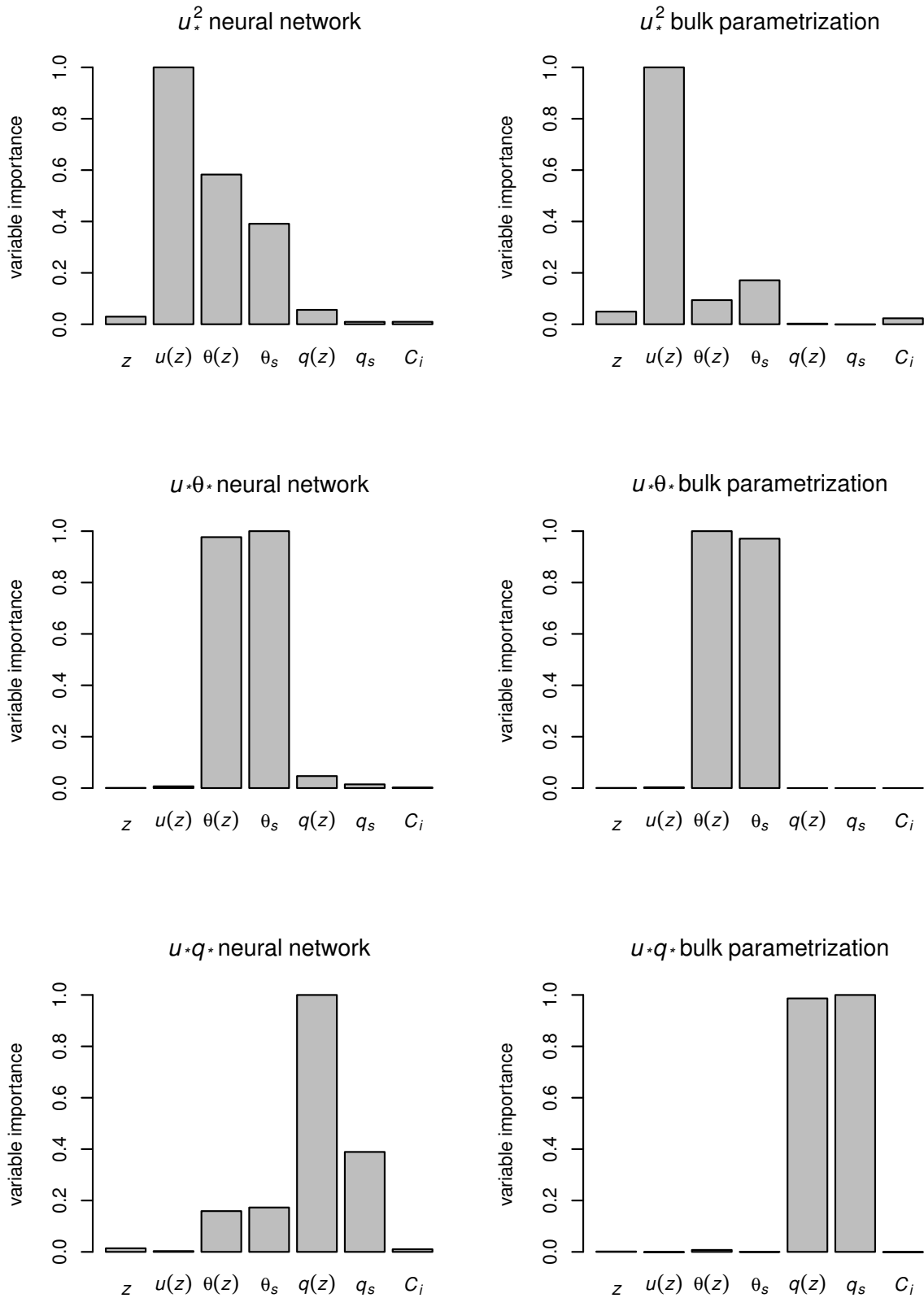


Figure 3: Bar plots showing the relative importance of the different input variables to the bulk algorithm and neural-network models. Variable importance metrics were computed using the “feature importance” algorithm of Breiman (2001).

407 The neural-network parametrization of the sensible heat flux $u_*\theta_*$ was generally suc-
 408 cessful, yielding reductions in RMSE of 12 % for the AO16 data and for two of the SHEBA
 409 PAM stations. For the ACSE dataset, and to a far greater extent ACCACIA, performance
 410 of the neural networks was worse. This is again a consequence of extrapolation failure. In
 411 ACCACIA, not only do all observations lie outside the range of z in the training set, but
 412 the observed fluxes themselves are often of much greater magnitude: the largest value of
 413 $u_*\theta_*$ in ACCACIA is more than five times larger than anything seen elsewhere. In both
 414 ACCACIA and ACSE, the neural networks systematically underestimate the magnitude
 415 of the extreme fluxes. This is because the use of a sigmoid activation function means the
 416 neural-network predictions will extrapolate roughly linearly until such a point as all the
 417 sigmoid activations on all the relevant neurons are saturated, after which the predictions
 418 will be insensitive to more extreme data. In this sense, the neural-network predictions
 419 in unseen conditions may be considered conservative estimates, as can be seen in Fig-
 420 ure 2. On the other hand, the bulk algorithm suffered no such intrinsic limitation in
 421 the magnitude of its flux predictions. The high correlation between the observed and
 422 bulk-estimated fluxes in ACCACIA and ACSE is largely due to co-occurrence of large
 423 positive or negative fluxes. There was an anomalously low correlation between observed
 424 and modelled (both bulk and neural-network) fluxes at the SHEBA Cleveland-Seattle-
 425 Maui PAM station. The Seattle site in particular was surrounded by ice ridging and the
 426 PAM station was downwind of a pressure ridge that disturbed the turbulence (Andreas
 427 et al., 2010a), so conditions there were not representative of those at the other sites.

428 Unlike the parametrizations of u_*^2 and $u_*\theta_*$, the neural-network estimator of the la-
 429 tent heat flux u_*q_* did not deliver performance improvements over the bulk algorithm,
 430 although for ACSE and AO16 performance of the two methods was similar. It should
 431 be noted that observed fluxes of latent heat are not available at the SHEBA PAM sta-
 432 tions, rendering the training sets in the cross-validation experiments both smaller and
 433 less representative of the corresponding validation sets. Latent heat flux observations
 434 in the Arctic are comparatively scarce, and of those available in this study the SHEBA
 435 tower contributes 94 %. The range of flux magnitudes observed at the SHEBA tower is

436 small in comparison to the other datasets. Encouragingly, where the training sets are
437 representative of conditions in the validation set (ACSE and AO16), performance of the
438 neural networks is on par with that of the bulk. Given some of the performance gains
439 of the neural-network parametrizations of u_{\star}^2 and $u_{\star}\theta_{\star}$, we might reasonably expect a
440 training set which samples densely a wider range of flux values to enable an improved
441 latent heat flux parametrization. Note, however, that the bulk algorithm generally per-
442 forms worse for $u_{\star}q_{\star}$ than for the other fluxes, a finding consistent with results obtained
443 outside the polar regions (e.g. McCandless et al., 2022). For example, it systematically
444 under-predicts those fluxes with larger magnitudes.

445 Results from the variable importance analysis illustrate some of the differences in how
446 the bulk algorithm and neural networks make use of their respective inputs (see Figure
447 3). For u_{\star}^2 , the primary difference is that the neural-network model is more sensitive to
448 the temperature inputs, as well as to the air humidity. The differences for $u_{\star}\theta_{\star}$ are less
449 pronounced; however, the neural-network model is relatively more sensitive to the non-
450 temperature inputs. For $u_{\star}q_{\star}$, the neural networks are less sensitive to surface humidity
451 than to air humidity, but also have a stronger dependence on the temperature inputs.
452 Due to the way it is constructed, the variable importance metric can be interpreted as
453 a measure of robustness to error in the various inputs. It is therefore unsurprising that
454 the accuracy of the bulk algorithm depends critically on the relevant gradient variables
455 for each flux. Note that the variable importance metric is strictly relative, so even a
456 very low score does not necessarily imply that an input is uninformative in an absolute
457 sense. Perhaps because they are trained on noisy observational data, the neural networks
458 appear to possess more redundancy across important inputs. For example, in the case of
459 $u_{\star}q_{\star}$, surface temperature θ_s is an excellent proxy variable from which to estimate surface
460 humidity q_s .

5 Summary and future directions

As the rapid melting of Arctic sea ice continues unabated, and as we become increasingly aware of the serious consequences of warming in the polar regions, the need for accurate representations of the relevant heat-transfer processes in climate models is greater than ever. Surface turbulent fluxes are a key mechanism for heat transfer between the atmosphere and ocean / sea ice, and yet their parametrization in current-generation climate models is based on traditional bulk formulae, originally calibrated in the tropics and mid-latitudes. Although polar-specific bulk formulations have been developed, their adoption in GCMs has been limited, in part due to the small number of field observations against which to validate their performance, and also because of difficulties modelling stable boundary layers generally.

The data-driven or machine-learning approach to parametrization of surface turbulent fluxes has emerged in recent years as an alternative or complement to bulk algorithms. In this study, it has been proposed to encode in a machine-learning model the relationships observed in practice between surface fluxes and meteorological predictor variables in the Arctic. To investigate feasibility of the data-driven approach, we have trained neural-network models using a database of observations assembled from several Arctic field campaigns. A bulk-algorithm implementation, containing advanced polar-specific parametrizations from the literature, has been used as a benchmark against which to test performance of machine-learning models.

Using a cross-validation scheme, the out-of-sample predictive accuracies of the bulk and neural-network parametrizations have been objectively compared. The neural-network parametrizations of the momentum and sensible heat fluxes were found to match and in some cases outperform their bulk counterparts in a RMSE sense. However, the neural-network latent heat flux parametrization was less successful and was generally outperformed by the bulk algorithm, probably due to insufficiently informative training data.

These results are encouraging and suggest directions for future research. Firstly, it may be possible to improve performance of the data-driven latent heat flux parametrization using observations from the recent MOSAiC campaign, where a large volume of data

490 has been collected (Shupe et al., 2022). We would expect an expanded training dataset
491 containing more extreme values to improve the representation of large fluxes. With the
492 MOSAiC data, it may be possible to investigate sea ice surface characteristics (e.g. ridges,
493 level ice, refrozen leads) as potential inputs to our algorithm. Another question to inves-
494 tigate is whether the bulk parametrization of latent heat flux can be used to inform or
495 constrain neural-network training in a hybrid parametrization approach: incorporation
496 of physical constraints has already been found to improve the extrapolation capability of
497 machine-learning models (Zhao et al., 2019). There is also the question of whether results
498 obtained here can be extended to sea ice in the Southern Ocean. Finally, having already
499 obtained promising data-driven parametrizations of momentum and sensible heat flux,
500 an immediate next step is to implement these models in a GCM. This step will likely
501 be non-trivial: due to compensating errors, better agreement with in-situ observations
502 is no guarantee that a new turbulence parametrization will improve predictive skill of
503 the GCM (Sandu et al., 2013). Implementation in a GCM may benefit from *equation*
504 *discovery* techniques (e.g. AI Feynman, Udrescu and Tegmark, 2020), whereby explicit
505 equations are found which approximate well the neural networks. Explicit equations
506 could reduce computational cost and would enable easier diagnostics in the case of model
507 crashes. Sensitivity studies with a GCM will allow us to assess the impact of these new
508 parametrizations on the polar atmosphere and on the melting of sea ice.

509 **Acknowledgements**

510 This is a contribution to the Year of Polar Prediction (YOPP), a flagship activity of the
511 Polar Prediction Project (PPP), initiated by the World Weather Research Programme
512 (WWRP) of the World Meteorological Organisation (WMO). We acknowledge the WMO
513 WWRP for its role in coordinating this international research activity.

514 The SHEBA data were provided by NCAR/EOL under the sponsorship of the Na-
515 tional Science Foundation. We gratefully acknowledge the SHEBA Atmospheric Surface
516 Flux Group (ASFG), who were responsible for the surface flux measurements during the

517 SHEBA project (E. L. Andreas, C. W. Fairall, P. S. Guest and P. O. G. Persson).

518 The neural-network architecture schematic in Figure 1 was created using the `plotnet`
519 function in the *NeuralNetTools* package for R (Beck, 2018). Fitting of neural-network
520 ensembles was automated with the help of wrapper functions in the R package *caret*
521 (Kuhn and Johnson, 2013). Bootstrapped significance testing of performance-metric
522 differences was performed using the R package *boot* (Canty and Ripley, 2022; Davison
523 and Hinkley, 1997).

524 We thank the three anonymous reviewers for their thoughtful comments and sugges-
525 tions, which helped improve the manuscript.

526 **Declarations**

527 **Ethical approval**

528 This declaration is not applicable.

529 **Competing interests**

530 The authors declare that they have no competing interests.

531 **Authors' contributions**

532 IMB, IAR, ADE and JP provided the ACCACIA, ACSE and AO16 data. VG built a
533 local database from all the observational campaigns and implemented the bulk algorithm
534 in Python. VG and SB advised on the bulk methodology and physical choices. DPC
535 carried out all the analyses. DPC wrote the article with VG. All authors reviewed and
536 provided feedback on the manuscript.

537 **Funding**

538 This work was supported by a national funding by the Agence Nationale de la Recherche
539 within the framework of the Investissement d'Avenir programme under the ANR-17-

540 MPGA-0003 ASET reference.

541 This article has received funding from the European Union’s Horizon 2020 research
542 and innovation programme under grant agreement No 101003826 via project CRiceS
543 (Climate Relevant interactions and feedbacks: the key role of sea ice and Snow in the
544 polar and global climate system).

545 The ACCACIA field campaign was supported by the UK Natural Environment Re-
546 search Council (NERC) grant numbers NE/I028653/1, NE/I028858/1, and NE/I028297/1.

547 The participation of Ian Brooks and John Prytherch in the ACSE field campaign was
548 supported by NERC grant number NE/K011820/1.

549 The AO16 measurements were supported by the the Swedish Polar Research Secre-
550 tariat. John Prytherch was also supported by the Knut and Alice Wallenberg Foundation
551 (grant number 2016-0024).

552 **Availability of data and materials**

553 **Code availability**

554 The polar-specific bulk algorithm used in this study and described in Section 3.1 is avail-
555 able to download as a Python library from GitHub ([https://github.com/virginieguemas/](https://github.com/virginieguemas/CDlib)
556 [CDlib](https://github.com/virginieguemas/CDlib)).

557 **Data availability**

558 **ACCACIA** flight data are available from the CEDA archive:

- 559 • <https://doi.org/10.5285/0844186db1ba9e20319a2560f8d61651> (MASIN);
- 560 • <https://catalogue.ceda.ac.uk/uuid/c064b0c150274a1cbd18c563573f392e> (FAAM).

561 **ACSE** cruise data are available from the CEDA archive ([https://doi.org/10.5285/](https://doi.org/10.5285/c6f1b1ff16f8407386e2d643bc5b916a)
562 [c6f1b1ff16f8407386e2d643bc5b916a](https://doi.org/10.5285/c6f1b1ff16f8407386e2d643bc5b916a), Brooks et al., 2022a).

563 **AO16** cruise data are available from the CEDA archive ([https://doi.org/10.5285/](https://doi.org/10.5285/614752d35dc147a598d5421443fb50e8)
564 [614752d35dc147a598d5421443fb50e8](https://doi.org/10.5285/614752d35dc147a598d5421443fb50e8), Brooks et al., 2022b).

565 **SHEBA** data are available from the NCAR Earth Observing Laboratory:

- 566 • (<https://doi.org/10.5065/D65H7DNS>, Andreas et al., 2007) (ASFG tower);
- 567 • (<https://doi.org/10.5065/D6ZC8170>, Andreas et al., 2012) (PAM stations).

568 **NSIDC** sea ice concentration data are available from the NSIDC archive ([https://](https://doi.org/10.7265/efmz-2t65)
569 doi.org/10.7265/efmz-2t65, Meier et al., 2021).

570 **A Polar-specific bulk parametrizations**

571 **A.1 Stability correction of Grachev et al. (2007)**

572 Grachev et al. (2007) assumed the form of the vertical profiles to be:

$$a(z) = p_1(\ln z)^2 + p_2 \ln(z) + p_3, \quad (8)$$

where a can be the wind speed, potential temperature, specific humidity, or any other variable, and p_1, p_2, p_3 are constants to be determined. By taking the derivative of eqn (8), the vertical gradients can be obtained through a fit to observations. Using data from the SHEBA tower, Grachev et al. (2007) proposed the “SHEBA profile functions”:

$$\phi_M = 1 + \frac{6.5\zeta(1 + \zeta)^{\frac{1}{3}}}{1.3 + \zeta}, \quad (9)$$

$$\phi_H = 1 + \frac{5\zeta + 5\zeta^2}{1 + 3\zeta + \zeta^2}, \quad (10)$$

573 where ζ is the Monin-Obukhov stability parameter and ϕ_M, ϕ_H are the non-dimensional
574 stability profile functions for momentum and sensible/latent heat respectively.

575 **A.2 Aerodynamic roughness model of Andreas et al. (2010b)**

576 Based on the SHEBA winter data, Andreas et al. (2010b) concluded that the aerodynamic
577 roughness z_0 did not significantly depend on the atmospheric stability. They proposed
578 the following unified parametrization:

$$z_0 = 0.135 \frac{\nu}{u_*} + B \tanh^3(13u_*), \quad (11)$$

579 where ν is the kinematic viscosity of air in m^2s^{-1} and $B = 2.3 \times 10^{-4}$. The first term on the
580 right models aerodynamically smooth regimes, while the second treats aerodynamically
581 rough regimes as well as the transition from smooth to rough flows.

582 **A.3 Scalar roughness model of Andreas (1987)**

583 Andreas (1987) proposed modelling the ratio of the scalar and aerodynamic roughness
584 lengths as a function of the roughness Reynolds number:

$$\ln \frac{z_s}{z_0} = b_{0,s} + b_{1,s} \ln R_* + b_{2,s} (\ln R_*)^2, \quad (12)$$

585 where z_s is the scalar roughness for temperature ($s = T$) or humidity ($s = Q$) and
586 $R_* = \frac{u_* z_0}{\nu}$ is the roughness Reynolds number. Polynomial coefficients $b_{i,s}$ are tabulated
587 for smooth ($R_* \leq 0.135$), transitional ($0.135 < R_* < 2.5$) and rough ($2.5 \leq R_* < 1000$)
588 surfaces in Andreas (1987).

589 **A.4 Form drag parametrization**

590 The form drag parametrization used in this study assumes that the drag coefficient C_D
591 in eqn (1) (the bulk exchange coefficient for momentum) can be partitioned as:

$$C_D = C_{D,w}(1 - C_i) + C_{D,i}C_i + C_{D,f}, \quad (13)$$

592 where $C_{D,w}$ and $C_{D,i}$ denote the skin drag coefficients over water and ice respectively, C_i
 593 is the sea ice concentration, and $C_{D,f}$ is the form drag contribution. We obtain $C_{D,f}$ by
 594 applying a stability correction to its neutral counterpart $C_{DN,f}$:

$$C_{DN,f} = C_{DN,f,w}(1 - C_i) + C_{DN,f,i}C_i, \quad (14)$$

595 where $C_{DN,f,k}$ are form-induced drag coefficients over water ($k = w$) and ice ($k = i$).
 596 Following Lüpkes et al. (2012) and Lüpkes and Gryanik (2015), we use:

$$C_{DN,f,k} = \frac{c_e}{2} \left[\frac{\ln \frac{h_{fc}}{z_{0,k}}}{\ln \frac{10}{z_{0,k}}} \right]^2 \frac{h_{fc}}{D} (1 - C_i)^\beta C_i, \quad (15)$$

597 where $c_e = 0.4$ is the effective resistance coefficient, $h_{fc} = 0.41$ m is the ice floe freeboard,
 598 $z_{0,k}$ is the skin drag aerodynamic roughness over water/ice, $D = 8$ m is the average
 599 diameter of leads or melt ponds and $\beta = 1$ is an optional exponent.

600 References

- 601 Andreas, E. L. (1987). A theory for the scalar roughness and the scalar transfer coefficients
 602 over snow and sea ice. *Boundary-Layer Meteorology*, 38(1):159–184.
- 603 Andreas, E. L. (1998). The Atmospheric Boundary Layer Over Polar Marine Surfaces. In
 604 Leppäranta, M., editor, *Physics of Ice-Covered Seas*, volume 2, pages 715–773. Helsinki
 605 University Press, Helsinki.
- 606 Andreas, E. L. (2011). A relationship between the aerodynamic and physical roughness of
 607 winter sea ice. *Quarterly Journal of the Royal Meteorological Society*, 137(659):1581–
 608 1588.
- 609 Andreas, E. L., Claffey, K. J., Jordan, R. E., Fairall, C. W., Guest, P. S., Persson, P.
 610 O. G., and Grachev, A. A. (2006). Evaluations of the von Kármán constant in the
 611 atmospheric surface layer. *Journal of Fluid Mechanics*, 559:117–149.

612 Andreas, E. L., Fairall, C., Guest, P., and Persson, O. (2007). Tower, 5-level hourly
613 measurements plus radiometer and surface data at Met City (ASFG). Version 1.0.

614 Andreas, E. L., Fairall, C., Guest, P., and Persson, O. (2012). Ice Camp Surface Mesonet
615 NCAR PAM-III 1 hour (FINAL). Version 1.0.

616 Andreas, E. L., Fairall, C. W., Grachev, A. A., Guest, P. S., Horst, T. W., Jordan,
617 R. E., and Persson, P. O. G. (2003). Turbulent transfer coefficients and roughness
618 lengths over sea ice: The SHEBA results. In *7th Conference on Polar Meteorology and*
619 *Oceanography. Hyannis, MA, Amer. Meteorol. Soc., Proc.*

620 Andreas, E. L., Fairall, C. W., Guest, P. S., and Persson, P. O. G. (1999). An overview
621 of the SHEBA atmospheric surface flux program. In *13th Symposium on Boundary*
622 *Layers and Turbulence. Dallas, TX, Amer. Meteorol. Soc., Proc.*, pages 550–555.

623 Andreas, E. L., Guest, P. S., Persson, P. O. G., Fairall, C. W., Horst, T. W., Moritz,
624 R. E., and Semmer, S. R. (2002). Near-surface water vapor over polar sea ice is always
625 near ice saturation. *Journal of Geophysical Research: Oceans*, 107(C10):SHE 8–1–SHE
626 8–15.

627 Andreas, E. L., Horst, T. W., Grachev, A. A., Persson, P. O. G., Fairall, C. W., Guest,
628 P. S., and Jordan, R. E. (2010a). Parametrizing turbulent exchange over summer sea
629 ice and the marginal ice zone. *Quarterly Journal of the Royal Meteorological Society*,
630 136(649):927–943.

631 Andreas, E. L., Persson, P. O. G., Grachev, A. A., Jordan, R. E., Horst, T. W., Guest,
632 P. S., and Fairall, C. W. (2010b). Parameterizing Turbulent Exchange over Sea Ice in
633 Winter. *Journal of Hydrometeorology*, 11(1):87–104.

634 Audouin, O., Roehrig, R., Couvreux, F., and Williamson, D. (2021). Modeling the
635 GABLS4 Strongly-Stable Boundary Layer With a GCM Turbulence Parameterization:
636 Parametric Sensitivity or Intrinsic Limits? *Journal of Advances in Modeling Earth*
637 *Systems*, 13(3):e2020MS002269.

- 638 Baas, P., Steeneveld, G. J., van de Wiel, B. J. H., and Holtslag, A. a. M. (2006). Explor-
639 ing Self-Correlation in Flux–Gradient Relationships for Stably Stratified Conditions.
640 *Journal of the Atmospheric Sciences*, 63(11):3045–3054.
- 641 Beck, M. W. (2018). NeuralNetTools: Visualization and Analysis Tools for Neural Net-
642 works. *Journal of Statistical Software*, 85:1–20.
- 643 Beljaars, A. C. M. and Holtslag, A. a. M. (1991). Flux Parameterization over Land
644 Surfaces for Atmospheric Models. *Journal of Applied Meteorology and Climatology*,
645 30(3):327–341.
- 646 Bonan, D. B., Lehner, F., and Holland, M. M. (2021a). Partitioning uncertainty in
647 projections of Arctic sea ice. *Environmental Research Letters*, 16(4):044002.
- 648 Bonan, D. B., Schneider, T., Eisenman, I., and Wills, R. C. J. (2021b). Constraining
649 the Date of a Seasonally Ice-Free Arctic Using a Simple Model. *Geophysical Research*
650 *Letters*, 48(18):e2021GL094309.
- 651 Bosveld, F. C., Baas, P., Steeneveld, G.-J., Holtslag, A. A. M., Angevine, W. M., Bazile,
652 E., de Bruijn, E. I. F., Deacu, D., Edwards, J. M., Ek, M., Larson, V. E., Pleim, J. E.,
653 Raschendorfer, M., and Svensson, G. (2014). The Third GABLS Intercomparison
654 Case for Evaluation Studies of Boundary-Layer Models. Part B: Results and Process
655 Understanding. *Boundary-Layer Meteorology*, 152(2):157–187.
- 656 Breiman, L. (2001). Random Forests. *Machine Learning*, 45(1):5–32.
- 657 Brooks, I. M., Prytherch, J., and Srivastava, P. (2022a). CANDIFLOS : Surface fluxes
658 from ACSE measurement campaign on icebreaker Oden, 2014.
- 659 Brooks, I. M., Prytherch, J., and Srivastava, P. (2022b). CANDIFLOS : Surface fluxes
660 from AO2016 measurement campaign on icebreaker Oden, 2014.
- 661 Broyden, C. G. (1970). The Convergence of a Class of Double-rank Minimization Algo-
662 rithms 1. General Considerations. *IMA Journal of Applied Mathematics*, 6(1):76–90.

- 663 Canty, A. and Ripley, B. D. (2022). Boot: Bootstrap Functions (Originally by Angelo
664 Canty for S).
- 665 Chen, T. and Guestrin, C. (2016). XGBoost: A Scalable Tree Boosting System. In
666 *Proceedings of the 22nd ACM SIGKDD International Conference on Knowledge Dis-*
667 *covery and Data Mining*, KDD '16, pages 785–794, New York, NY, USA. Association
668 for Computing Machinery.
- 669 Cohen, J., Screen, J. A., Furtado, J. C., Barlow, M., Whittleston, D., Coumou, D.,
670 Francis, J., Dethloff, K., Entekhabi, D., Overland, J., and Jones, J. (2014). Recent
671 Arctic amplification and extreme mid-latitude weather. *Nature Geoscience*, 7(9):627–
672 637.
- 673 Cohen, J., Zhang, X., Francis, J., Jung, T., Kwok, R., Overland, J., Ballinger, T. J.,
674 Bhatt, U. S., Chen, H. W., Coumou, D., Feldstein, S., Gu, H., Handorf, D., Henderson,
675 G., Ionita, M., Kretschmer, M., Laliberte, F., Lee, S., Linderholm, H. W., Maslowski,
676 W., Peings, Y., Pfeiffer, K., Rigor, I., Semmler, T., Stroeve, J., Taylor, P. C., Vavrus,
677 S., Vihma, T., Wang, S., Wendisch, M., Wu, Y., and Yoon, J. (2020). Divergent
678 consensuses on Arctic amplification influence on midlatitude severe winter weather.
679 *Nature Climate Change*, 10(1):20–29.
- 680 Cuxart, J., Holtslag, A. A. M., Beare, R. J., Bazile, E., Beljaars, A., Cheng, A., Conangla,
681 L., Ek, M., Freedman, F., Hamdi, R., Kerstein, A., Kitagawa, H., Lenderink, G.,
682 Lewellen, D., Mailhot, J., Mauritsen, T., Perov, V., Schayes, G., Steeneveld, G.-J.,
683 Svensson, G., Taylor, P., Weng, W., Wunsch, S., and Xu, K.-M. (2006). Single-Column
684 Model Intercomparison for a Stably Stratified Atmospheric Boundary Layer. *Boundary-*
685 *Layer Meteorology*, 118(2):273–303.
- 686 Davison, A. C. and Hinkley, D. V. (1997). *Bootstrap Methods and Their Application*.
687 Cambridge Series in Statistical and Probabilistic Mathematics. Cambridge University
688 Press, Cambridge.
- 689 Edson, J. B., Jampana, V., Weller, R. A., Bigorre, S. P., Plueddemann, A. J., Fairall,

690 C. W., Miller, S. D., Mahrt, L., Vickers, D., and Hersbach, H. (2013). On the Exchange
691 of Momentum over the Open Ocean. *Journal of Physical Oceanography*, 43(8):1589–
692 1610.

693 Edson, J. B., Zappa, C. J., Ware, J. A., McGillis, W. R., and Hare, J. E. (2004). Scalar
694 flux profile relationships over the open ocean. *Journal of Geophysical Research: Oceans*,
695 109(C8).

696 Elvidge, A. D., Renfrew, I., Edwards, J., Brooks, I., Srivastava, P., and Weiss, A. (2023).
697 Improved simulation of the polar atmospheric boundary layer by accounting for aero-
698 dynamic roughness in the parameterisation of surface scalar exchange over sea ice.
699 *Journal of Advances in Modeling Earth Systems*.

700 Elvidge, A. D., Renfrew, I. A., Brooks, I. M., Srivastava, P., Yelland, M. J., and Pry-
701 therch, J. (2021). Surface Heat and Moisture Exchange in the Marginal Ice Zone:
702 Observations and a New Parameterization Scheme for Weather and Climate Models.
703 *Journal of Geophysical Research: Atmospheres*, 126(17):e2021JD034827.

704 Elvidge, A. D., Renfrew, I. A., Weiss, A. I., Brooks, I. M., Lachlan-Cope, T. A., and
705 King, J. C. (2016). Observations of surface momentum exchange over the marginal
706 ice zone and recommendations for its parametrisation. *Atmospheric Chemistry and*
707 *Physics*, 16(3):1545–1563.

708 Fairall, C. W., Bradley, E. F., Hare, J. E., Grachev, A. A., and Edson, J. B. (2003).
709 Bulk Parameterization of Air–Sea Fluxes: Updates and Verification for the COARE
710 Algorithm. *Journal of Climate*, 16(4):571–591.

711 Fiedler, E. K., Lachlan-Cope, T. A., Renfrew, I. A., and King, J. C. (2010). Convective
712 heat transfer over thin ice covered coastal polynyas. *Journal of Geophysical Research:*
713 *Oceans*, 115(C10).

714 Fletcher, R. (1970). A new approach to variable metric algorithms. *The Computer*
715 *Journal*, 13(3):317–322.

- 716 Friedman, J. H. (1991). Multivariate Adaptive Regression Splines. *The Annals of Statis-*
717 *tics*, 19(1):1–67.
- 718 Friedman, J. H. (2001). Greedy function approximation: A gradient boosting machine.
719 *The Annals of Statistics*, 29(5):1189–1232.
- 720 Garratt, J. R. (1994). *The Atmospheric Boundary Layer*. Cambridge Atmospheric and
721 Space Science Series. Cambridge University Press, Cambridge, UK.
- 722 Gascard, J.-C., Zhang, J., and Rafizadeh, M. (2019). Rapid decline of Arctic sea ice
723 volume: Causes and consequences. *The Cryosphere Discussions*, pages 1–29.
- 724 Goldfarb, D. (1970). A family of variable-metric methods derived by variational means.
725 *Mathematics of Computation*, 24(109):23–26.
- 726 Grachev, A. A., Andreas, E. L., Fairall, C. W., Guest, P. S., and Persson, P. O. G.
727 (2007). SHEBA flux–profile relationships in the stable atmospheric boundary layer.
728 *Boundary-Layer Meteorology*, 124(3):315–333.
- 729 Grachev, A. A. and Fairall, C. W. (1997). Dependence of the Monin–Obukhov Stabil-
730 ity Parameter on the Bulk Richardson Number over the Ocean. *Journal of Applied*
731 *Meteorology and Climatology*, 36(4):406–414.
- 732 Grachev, A. A., Fairall, C. W., and Bradley, E. F. (2000). Convective Profile Constants
733 Revisited. *Boundary-Layer Meteorology*, 94(3):495–515.
- 734 Grachev, A. A., Fairall, C. W., Persson, P. O. G., Andreas, E. L., and Guest, P. S.
735 (2002). Stable boundary-layer regimes observed during the SHEBA Experiment. In
736 *15th Symposium on Boundary Layers and Turbulence. Wageningen, The Netherlands,*
737 *Amer. Meteorol. Soc., Proc.*, pages 374–377.
- 738 Grachev, A. A., Fairall, C. W., Persson, P. O. G., Andreas, E. L., and Guest, P. S.
739 (2005). Stable Boundary-Layer Scaling Regimes: The SHEBA Data. *Boundary-Layer*
740 *Meteorology*, 116(2):201–235.

- 741 Graversen, R. G., Mauritsen, T., Tjernström, M., Källén, E., and Svensson, G. (2008).
742 Vertical structure of recent Arctic warming. *Nature*, 451(7174):53–56.
- 743 Hastie, T. and Tibshirani, R. (1986). Generalized Additive Models. *Statistical Science*,
744 1(3):297–310.
- 745 Hastie, T., Tibshirani, R., and Friedman, J. (2009). Neural Networks. In Hastie, T., Tib-
746 shirani, R., and Friedman, J., editors, *The Elements of Statistical Learning: Data Min-
747 ing, Inference, and Prediction*, Springer Series in Statistics, pages 389–416. Springer,
748 New York, NY.
- 749 Hornik, K., Stinchcombe, M., and White, H. (1989). Multilayer feedforward networks are
750 universal approximators. *Neural Networks*, 2(5):359–366.
- 751 Jung, T., Doblas-Reyes, F., Goessling, H., Guemas, V., Bitz, C., Buontempo, C., Ca-
752 ballero, R., Jakobson, E., Jungclaus, J., Karcher, M., Koenigk, T., Matei, D., Overland,
753 J., Spengler, T., and Yang, S. (2015). Polar Lower-Latitude Linkages and Their Role
754 in Weather and Climate Prediction. *Bulletin of the American Meteorological Society*,
755 96(11):ES197–ES200.
- 756 Jung, T., Gordon, N. D., Bauer, P., Bromwich, D. H., Chevallier, M., Day, J. J., Dawson,
757 J., Doblas-Reyes, F., Fairall, C., Goessling, H. F., Holland, M., Inoue, J., Iversen, T.,
758 Klebe, S., Lemke, P., Losch, M., Makshtas, A., Mills, B., Nurmi, P., Perovich, D.,
759 Reid, P., Renfrew, I. A., Smith, G., Svensson, G., Tolstykh, M., and Yang, Q. (2016).
760 Advancing Polar Prediction Capabilities on Daily to Seasonal Time Scales. *Bulletin of
761 the American Meteorological Society*, 97(9):1631–1647.
- 762 King, J. C., Lachlan-Cope, T. A., Ladkin, R. S., and Weiss, A. (2008). Airborne Measure-
763 ments in the Stable Boundary Layer over the Larsen Ice Shelf, Antarctica. *Boundary-
764 Layer Meteorology*, 127(3):413–428.
- 765 Kovacs, K. M., Lydersen, C., Overland, J. E., and Moore, S. E. (2011). Impacts of chang-
766 ing sea-ice conditions on Arctic marine mammals. *Marine Biodiversity*, 41(1):181–194.

- 767 Krizhevsky, A., Sutskever, I., and Hinton, G. E. (2017). ImageNet classification with
768 deep convolutional neural networks. *Communications of the ACM*, 60(6):84–90.
- 769 Kuhn, M. and Johnson, K. (2013). *Applied Predictive Modeling*. Springer, New York,
770 NY.
- 771 Lesins, G., Duck, T. J., and Drummond, J. R. (2012). Surface Energy Balance Framework
772 for Arctic Amplification of Climate Change. *Journal of Climate*, 25(23):8277–8288.
- 773 Leufen, L. H. and Schädler, G. (2019). Calculating the turbulent fluxes in the atmospheric
774 surface layer with neural networks. *Geoscientific Model Development*, 12(5):2033–2047.
- 775 Liu, J., Song, M., Zhu, Z., Horton, R. M., Hu, Y., and Xie, S.-P. (2022). Arctic sea-ice loss
776 is projected to lead to more frequent strong El Niño events. *Nature Communications*,
777 13(1):4952.
- 778 Lüpkes, C. and Gryanik, V. M. (2015). A stability-dependent parametrization of transfer
779 coefficients for momentum and heat over polar sea ice to be used in climate models.
780 *Journal of Geophysical Research: Atmospheres*, 120(2):552–581.
- 781 Lüpkes, C., Gryanik, V. M., Hartmann, J., and Andreas, E. L. (2012). A parametriza-
782 tion, based on sea ice morphology, of the neutral atmospheric drag coefficients for
783 weather prediction and climate models. *Journal of Geophysical Research: Atmospheres*,
784 117(D13).
- 785 Lüpkes, C., Gryanik, V. M., Rösel, A., Birnbaum, G., and Kaleschke, L. (2013). Effect
786 of sea ice morphology during Arctic summer on atmospheric drag coefficients used in
787 climate models. *Geophysical Research Letters*, 40(2):446–451.
- 788 McCandless, T., Gagne, D. J., Kosović, B., Haupt, S. E., Yang, B., Becker, C., and
789 Schreck, J. (2022). Machine Learning for Improving Surface-Layer-Flux Estimates.
790 *Boundary-Layer Meteorology*, 185(2):199–228.
- 791 Meier, W. N., Fetterer, F., Windnagel, A., and Stewart, S. (2021). NOAA/NSIDC
792 Climate Data Record of Passive Microwave Sea Ice Concentration, Version 4.

793 Meier, W. N., Hovelsrud, G. K., van Oort, B. E., Key, J. R., Kovacs, K. M., Michel,
794 C., Haas, C., Granskog, M. A., Gerland, S., Perovich, D. K., Makshtas, A., and Reist,
795 J. D. (2014). Arctic sea ice in transformation: A review of recent observed changes
796 and impacts on biology and human activity. *Reviews of Geophysics*, 52(3):185–217.

797 Monin, A. S. and Obukhov, A. M. (1954). Basic laws of turbulent mixing in the surface
798 layer of the atmosphere. *Tr. Akad. Nauk SSSR Geophys. Inst.*, 24(151):163–187.

799 Muñoz-Esparza, D., Becker, C., Sauer, J. A., Gagne II, D. J., Schreck, J., and Kosović,
800 B. (2022). On the Application of an Observations-Based Machine Learning Parameter-
801 ization of Surface Layer Fluxes Within an Atmospheric Large-Eddy Simulation Model.
802 *Journal of Geophysical Research: Atmospheres*, 127(16):e2021JD036214.

803 Notz, D., Haumann, F. A., Haak, H., Jungclaus, J. H., and Marotzke, J. (2013). Arctic
804 sea-ice evolution as modeled by Max Planck Institute for Meteorology’s Earth system
805 model. *Journal of Advances in Modeling Earth Systems*, 5(2):173–194.

806 Pelliccioni, A., Poli, U., Agnello, P., and Coni, A. (1999). Application of neural networks
807 to model the Monin-Obukhov length and the mixed-layer height from ground-based
808 meteorological data. *Transactions on Ecology and the Environment*, 29:1055–1064.

809 Persson, O., Shupe, M. D., Tjernström, M., Sedlar, J., Brooks, I. M., Brooks, B. J., Bjork,
810 G., Prytherch, J., Salisbury, D., Achtert, P., Sotiropoulou, G., Johnston, P. E., and
811 Wolfe, D. (2015). ATMOSPHERE-ICE-OCEAN INTERACTIONS DURING SUM-
812 MER MELT AND EARLY AUTUMN FREEZE-UP: OBSERVATIONS FROM THE
813 ACSE FIELD PROGRAM.

814 Persson, P. O. G., Fairall, C. W., Andreas, E. L., Guest, P. S., and Perovich, D. K.
815 (2002). Measurements near the Atmospheric Surface Flux Group tower at SHEBA:
816 Near-surface conditions and surface energy budget. *Journal of Geophysical Research:*
817 *Oceans*, 107(C10):SHE 21–1–SHE 21–35.

818 Petersen, G. N. and Renfrew, I. A. (2009). Aircraft-based observations of air–sea fluxes

819 over Denmark Strait and the Irminger Sea during high wind speed conditions. *Quarterly*
820 *Journal of the Royal Meteorological Society*, 135(645):2030–2045.

821 Post, E., Bhatt, U. S., Bitz, C. M., Brodie, J. F., Fulton, T. L., Hebblewhite, M., Kerby,
822 J., Kutz, S. J., Stirling, I., and Walker, D. A. (2013). Ecological Consequences of
823 Sea-Ice Decline. *Science*, 341(6145):519–524.

824 Previdi, M., Smith, K. L., and Polvani, L. M. (2021). Arctic amplification of cli-
825 mate change: A review of underlying mechanisms. *Environmental Research Letters*,
826 16(9):093003.

827 Prytherch, J., Brooks, I. M., Crill, P. M., Thornton, B. F., Salisbury, D. J., Tjernström,
828 M., Anderson, L. G., Geibel, M. C., and Humborg, C. (2017). Direct determination of
829 the air-sea CO₂ gas transfer velocity in Arctic sea ice regions. *Geophysical Research*
830 *Letters*, 44(8):3770–3778.

831 Qin, Z., Su, G.-l., Yu, Q., Hu, B.-m., and Li, J. (2005a). Modeling water and carbon
832 fluxes above summer maize field in North China Plain with back-propagation neural
833 networks. *Journal of Zhejiang University-SCIENCE B*, 6(5):418–426.

834 Qin, Z., Yu, Q., Li, J., Wu, Z.-y., and Hu, B.-m. (2005b). Application of least squares
835 vector machines in modelling water vapor and carbon dioxide fluxes over a cropland.
836 *Journal of Zhejiang University-SCIENCE B*, 6(6):491–495.

837 R Core Team (2021). *R: A Language and Environment for Statistical Computing*. R
838 Foundation for Statistical Computing, Vienna, Austria.

839 Renfrew, I. A., Elvidge, A. D., and Edwards, J. M. (2019). Atmospheric sensitivity to
840 marginal-ice-zone drag: Local and global responses. *Quarterly Journal of the Royal*
841 *Meteorological Society*, 145(720):1165–1179.

842 Renfrew, I. A., Moore, G. W. K., Kristjánsson, J. E., Ólafsson, H., Gray, S. L., Petersen,
843 G. N., Bovis, K., Brown, P. R. A., Føre, I., Haine, T., Hay, C., Irvine, E. A., Lawrence,
844 A., Ohigashi, T., Outten, S., Pickart, R. S., Shapiro, M., Sproson, D., Swinbank,

- 845 R., Woolley, A., and Zhang, S. (2008). THE GREENLAND FLOW DISTORTION
846 EXPERIMENT. *Bulletin of the American Meteorological Society*, 89(9):1307–1324.
- 847 Ripley, B. D. (1996). Feed-forward Neural Networks. In *Pattern Recognition and Neural*
848 *Networks*, pages 143–180. Cambridge University Press, Cambridge.
- 849 Rothrock, D. A., Yu, Y., and Maykut, G. A. (1999). Thinning of the Arctic sea-ice cover.
850 *Geophysical Research Letters*, 26(23):3469–3472.
- 851 Safa, B., Arkebauer, T. J., Zhu, Q., Suyker, A., and Irmak, S. (2018). Latent heat and
852 sensible heat flux simulation in maize using artificial neural networks. *Computers and*
853 *Electronics in Agriculture*, 154:155–164.
- 854 Sandu, I., Beljaars, A., Bechtold, P., Mauritsen, T., and Balsamo, G. (2013). Why is
855 it so difficult to represent stably stratified conditions in numerical weather prediction
856 (NWP) models? *Journal of Advances in Modeling Earth Systems*, 5(2):117–133.
- 857 Screen, J. A. and Simmonds, I. (2010). The central role of diminishing sea ice in recent
858 Arctic temperature amplification. *Nature*, 464(7293):1334–1337.
- 859 Serreze, M. C., Barrett, A. P., Stroeve, J. C., Kindig, D. N., and Holland, M. M. (2009).
860 The emergence of surface-based Arctic amplification. *The Cryosphere*, 3(1):11–19.
- 861 Serreze, M. C. and Barry, R. G. (2011). Processes and impacts of Arctic amplification:
862 A research synthesis. *Global and Planetary Change*, 77(1):85–96.
- 863 Serreze, M. C. and Francis, J. A. (2006). The Arctic Amplification Debate. *Climatic*
864 *Change*, 76(3):241–264.
- 865 Shanno, D. F. (1970). Conditioning of quasi-Newton methods for function minimization.
866 *Mathematics of Computation*, 24(111):647–656.
- 867 Shupe, M. D., Rex, M., Blomquist, B., Persson, P. O. G., Schmale, J., Uttal, T., Al-
868 thausen, D., Angot, H., Archer, S., Bariteau, L., Beck, I., Bilberry, J., Bucci, S., Buck,
869 C., Boyer, M., Brasseur, Z., Brooks, I. M., Calmer, R., Cassano, J., Castro, V., Chu,

870 D., Costa, D., Cox, C. J., Creamean, J., Crewell, S., Dahlke, S., Damm, E., de Boer, G.,
 871 Deckelmann, H., Dethloff, K., Dütsch, M., Ebell, K., Ehrlich, A., Ellis, J., Engelmann,
 872 R., Fong, A. A., Frey, M. M., Gallagher, M. R., Ganzeveld, L., Gradinger, R., Graeser,
 873 J., Greenamyre, V., Griesche, H., Griffiths, S., Hamilton, J., Heinemann, G., Helmig,
 874 D., Herber, A., Heuzé, C., Hofer, J., Houchens, T., Howard, D., Inoue, J., Jacobi,
 875 H.-W., Jaiser, R., Jokinen, T., Jourdan, O., Jozef, G., King, W., Kirchgaessner, A.,
 876 Klingebiel, M., Krassovski, M., Krumpen, T., Lampert, A., Landing, W., Laurila, T.,
 877 Lawrence, D., Lonardi, M., Loose, B., Lüpkes, C., Maahn, M., Macke, A., Maslowski,
 878 W., Marsay, C., Maturilli, M., Mech, M., Morris, S., Moser, M., Nicolaus, M., Ortega,
 879 P., Osborn, J., Pätzold, F., Perovich, D. K., Petäjä, T., Pilz, C., Pirazzini, R., Pos-
 880 man, K., Powers, H., Pratt, K. A., Preußner, A., Quéléver, L., Radenz, M., Rabe, B.,
 881 Rinke, A., Sachs, T., Schulz, A., Siebert, H., Silva, T., Solomon, A., Sommerfeld, A.,
 882 Spreen, G., Stephens, M., Stohl, A., Svensson, G., Uin, J., Viegas, J., Voigt, C., von
 883 der Gathen, P., Wehner, B., Welker, J. M., Wendisch, M., Werner, M., Xie, Z., and
 884 Yue, F. (2022). Overview of the MOSAiC expedition: Atmosphere. *Elementa: Science*
 885 *of the Anthropocene*, 10(1):00060.

886 Sotiropoulou, G., Tjernström, M., Sedlar, J., Achtert, P., Brooks, B. J., Brooks, I. M.,
 887 Persson, P. O. G., Prytherch, J., Salisbury, D. J., Shupe, M. D., Johnston, P. E.,
 888 and Wolfe, D. (2016). Atmospheric Conditions during the Arctic Clouds in Summer
 889 Experiment (ACSE): Contrasting Open Water and Sea Ice Surfaces during Melt and
 890 Freeze-Up Seasons. *Journal of Climate*, 29(24):8721–8744.

891 Srivastava, P., Brooks, I. M., Prytherch, J., Salisbury, D. J., Elvidge, A. D., Renfrew,
 892 I. A., and Yelland, M. J. (2022). Ship-based estimates of momentum transfer coefficient
 893 over sea ice and recommendations for its parameterization. *Atmospheric Chemistry and*
 894 *Physics*, 22(7):4763–4778.

895 Svensson, G., Holtslag, A. A. M., Kumar, V., Mauritsen, T., Steeneveld, G. J., Angevine,
 896 W. M., Bazile, E., Beljaars, A., de Bruijn, E. I. F., Cheng, A., Conangla, L., Cuxart,
 897 J., Ek, M., Falk, M. J., Freedman, F., Kitagawa, H., Larson, V. E., Lock, A., Mailhot,

898 J., Masson, V., Park, S., Pleim, J., Söderberg, S., Weng, W., and Zampieri, M. (2011).
899 Evaluation of the Diurnal Cycle in the Atmospheric Boundary Layer Over Land as
900 Represented by a Variety of Single-Column Models: The Second GABLS Experiment.
901 *Boundary-Layer Meteorology*, 140(2):177–206.

902 Thornton, B. F., Prytherch, J., Andersson, K., Brooks, I. M., Salisbury, D., Tjernström,
903 M., and Crill, P. M. (2020). Shipborne eddy covariance observations of methane fluxes
904 constrain Arctic sea emissions. *Science Advances*, 6(5):eaay7934.

905 Tjernström, M. and Jakobsson, M. (2021). Data from expedition Arctic Ocean, 2016.

906 Tynan, E. (2015). Effects of sea-ice loss. *Nature Climate Change*, 5(7):621–621.

907 Udrescu, S.-M. and Tegmark, M. (2020). AI Feynman: A physics-inspired method for
908 symbolic regression. *Science Advances*, 6(16):eaay2631.

909 Uttal, T., Curry, J. A., McPhee, M. G., Perovich, D. K., Moritz, R. E., Maslanik, J. A.,
910 Guest, P. S., Stern, H. L., Moore, J. A., Turenne, R., Heiberg, A., Serreze, M. C.,
911 Wylie, D. P., Persson, O. G., Paulson, C. A., Halle, C., Morison, J. H., Wheeler,
912 P. A., Makshtas, A., Welch, H., Shupe, M. D., Intrieri, J. M., Stamnes, K., Lindsey,
913 R. W., Pinkel, R., Pegau, W. S., Stanton, T. P., and Grenfeld, T. C. (2002). Surface
914 Heat Budget of the Arctic Ocean. *Bulletin of the American Meteorological Society*,
915 83(2):255–276.

916 Venables, W. N. and Ripley, B. D. (2002). *Modern Applied Statistics with S*. Statistics
917 and Computing. Springer, New York, NY.

918 Vihma, T. (1995). Subgrid parameterization of surface heat and momentum fluxes over
919 polar oceans. *Journal of Geophysical Research: Oceans*, 100(C11):22625–22646.

920 Vihma, T., Pirazzini, R., Fer, I., Renfrew, I. A., Sedlar, J., Tjernström, M., Lüpkes, C.,
921 Nygård, T., Notz, D., Weiss, J., Marsan, D., Cheng, B., Birnbaum, G., Gerland, S.,
922 Chechin, D., and Gascard, J. C. (2014). Advances in understanding and parameteri-
923 zation of small-scale physical processes in the marine Arctic climate system: A review.
924 *Atmospheric Chemistry and Physics*, 14(17):9403–9450.

- 925 Voldoire, A., Saint-Martin, D., S en esi, S., Decharme, B., Alias, A., Chevallier, M., Colin,
926 J., Gu er emy, J.-F., Michou, M., Moine, M.-P., Nabat, P., Roehrig, R., Salas y M elia,
927 D., S ef erian, R., Valcke, S., Beau, I., Belamari, S., Berthet, S., Cassou, C., Cattiaux,
928 J., Deshayes, J., Douville, H., Eth e, C., Franchist eguy, L., Geoffroy, O., L evy, C.,
929 Madec, G., Meurdesoif, Y., Msadek, R., Ribes, A., Sanchez-Gomez, E., Terray, L., and
930 Waldman, R. (2019). Evaluation of CMIP6 DECK Experiments With CNRM-CM6-1.
931 *Journal of Advances in Modeling Earth Systems*, 11(7):2177–2213.
- 932 Wang, L., Zhang, Y., Yao, Y., Xiao, Z., Shang, K., Guo, X., Yang, J., Xue, S., and Wang,
933 J. (2021). GBRT-Based Estimation of Terrestrial Latent Heat Flux in the Haihe River
934 Basin from Satellite and Reanalysis Datasets. *Remote Sensing*, 13(6):1054.
- 935 Wang, X., Yao, Y., Zhao, S., Jia, K., Zhang, X., Zhang, Y., Zhang, L., Xu, J., and
936 Chen, X. (2017). MODIS-Based Estimation of Terrestrial Latent Heat Flux over North
937 America Using Three Machine Learning Algorithms. *Remote Sensing*, 9(12):1326.
- 938 Wulfmeyer, V., Pineda, J. M. V., Otte, S., Karlbauer, M., Butz, M. V., Lee, T. R., and
939 Rajtschan, V. (2022). Estimation of the Surface Fluxes for Heat and Momentum in
940 Unstable Conditions with Machine Learning and Similarity Approaches for the LAFE
941 Data Set. *Boundary-Layer Meteorology*.
- 942 Xu, T., Guo, Z., Liu, S., He, X., Meng, Y., Xu, Z., Xia, Y., Xiao, J., Zhang, Y., Ma, Y.,
943 and Song, L. (2018). Evaluating Different Machine Learning Methods for Upscaling
944 Evapotranspiration from Flux Towers to the Regional Scale. *Journal of Geophysical*
945 *Research: Atmospheres*, 123(16):8674–8690.
- 946 Zhao, W. L., Gentine, P., Reichstein, M., Zhang, Y., Zhou, S., Wen, Y., Lin, C., Li, X.,
947 and Qiu, G. Y. (2019). Physics-Constrained Machine Learning of Evapotranspiration.
948 *Geophysical Research Letters*, 46(24):14496–14507.